Supplementary Information for:
Tracking deep-time environmental stability exposes a global conservation gap

Pedro Cermeño*[1], Carmen García–Comas[1], Gloria Herrero–Gascón[1], Khushboo Gurung[2], Guillaume Le Gland[3], Benjamin Mills[2], Alexandre Pohl[4], Sergio Vallina[5], Simon Williams[6]

October, 7th, 2026

[1] Centro Mediterráneo de Investigaciones Marinas y Ambientales, Consejo Superior de Investigaciones Científicas, Passeig Marítim de la Barceloneta 37-49, Barcelona, 08003, Spain.
[2] School of Earth and Environment, The University of Leeds, Leeds, LS2 9JT, United Kingdom.
[3] Mediterranean Institute of Oceanography, 163 avenue de Luminy, 13288 Marseille Cedex 09, France.
[4] Université Bourgogne Europe, CNRS, Biogeosciences UMR6282, 21000 Dijon, France.
[5] Instituto Español de Oceanografía, Consejo Superior de Investigaciones Científicas, Gijón, 21000, Spain.
[6] Institute for Marine and Antarctic Studies, University of Tasmania, 20 Castray Esplanade, Battery Point, Hobart, TAS 7004, Australia.

* Corresponding author: pedrocermeno@icm.csic.es

Contents

SCION modelling **2**
Climatic simulations **7**
Climate velocity, plate motion and thermal mismatch through time **7**
Climate velocity 7
Plate motion as a modifier of the climate velocity 8
Interplay of plate tectonics and climate velocity 8
Choice of and sensitivity to the refugium threshold **12**
Supplementary References **17**
Supplementary Figs. S1–S12

SCION modelling

SCION is a global climate-biogeochemical model for deep time that uses a spatially resolved palaeogeographic and climate emulator to solve surface processes at the regional scale over multimillion-year timescales [1] (**Figure S1**). The model produces a self-consistent forwards-in-time estimate of the evolution of the global C–O–P–N–S cycles alongside spatially resolved climate. In this study, we use an existing dynamic coupling between SCION (version 1.3) and the FLORA deep-time vegetation model [2]. FLORA uses regional environmental parameters (runoff, insolation, temperature, and atmospheric CO_2 and O_2) to calculate terrestrial photosynthesis and carbon allocation following the LPJ dynamic global vegetation model [3], and these are recalculated at each SCION timestep, and inform land-derived organic carbon burial and continental weathering rates. Thus, the vegetation biogeography and biomass become part of a feedback loop that affects overall CO_2 and O_2 availability over deep time. We also modify the model by updating the climate emulator with information from new runs of the Fast Ocean Atmosphere Model (FOAM), using the palaeogeographic maps of Scotese and Wright [4], defined every 5 Myrs.

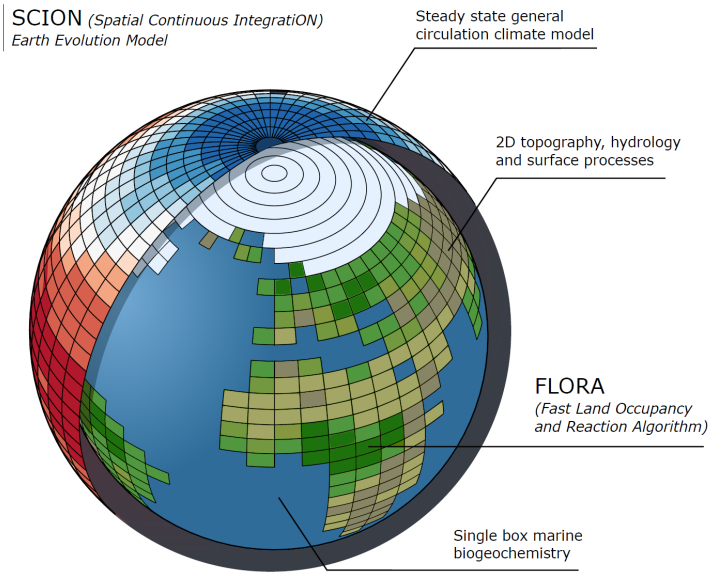


Figure S1. SCION-FLORA model linkage.

Although recent SCION versions, including linkages to FLORA, have succeeded in reproducing Phanerozoic-scale greenhouse-icehouse cycles and predicts Cenozoic cooling, the model does not map perfectly onto proxy temperature records for the Cenozoic. For this study, a close correspondence with proxy-determined Cenozoic global temperatures [5] is required, so we use a model inversion approach to modify the global rate of tectonic CO_2 degassing such that the model produces a reasonable broad-timescale picture of Cenozoic cooling, while maintaining a self-consistent prediction of the biomass and distribution of vegetation. This requires a ~35% reduction in CO_2 degassing rates over the Cenozoic, which is at the upper end of recent estimates for combined tectonic degassing over this period [6]. It also requires that modern degassing rates are maintained around 40% higher than the previously-assumed rate, because the FOAM GCM has a preindustrial global average surface temperature of around 13 °C, compared to the 14 °C in the proxy record. This leaves the model present day CO_2 levels elevated at around 400 ppm, which also drives elevated O_2 at around 25.5% atm, due to regulation of CO_2/O_2 levels by the terrestrial and marine photosynthetic biospheres. Due to low climate sensitivity in FOAM, the model also predicts a Cenozoic CO_2 level that is broadly similar in trend but above proxy values (**Figure S2**).

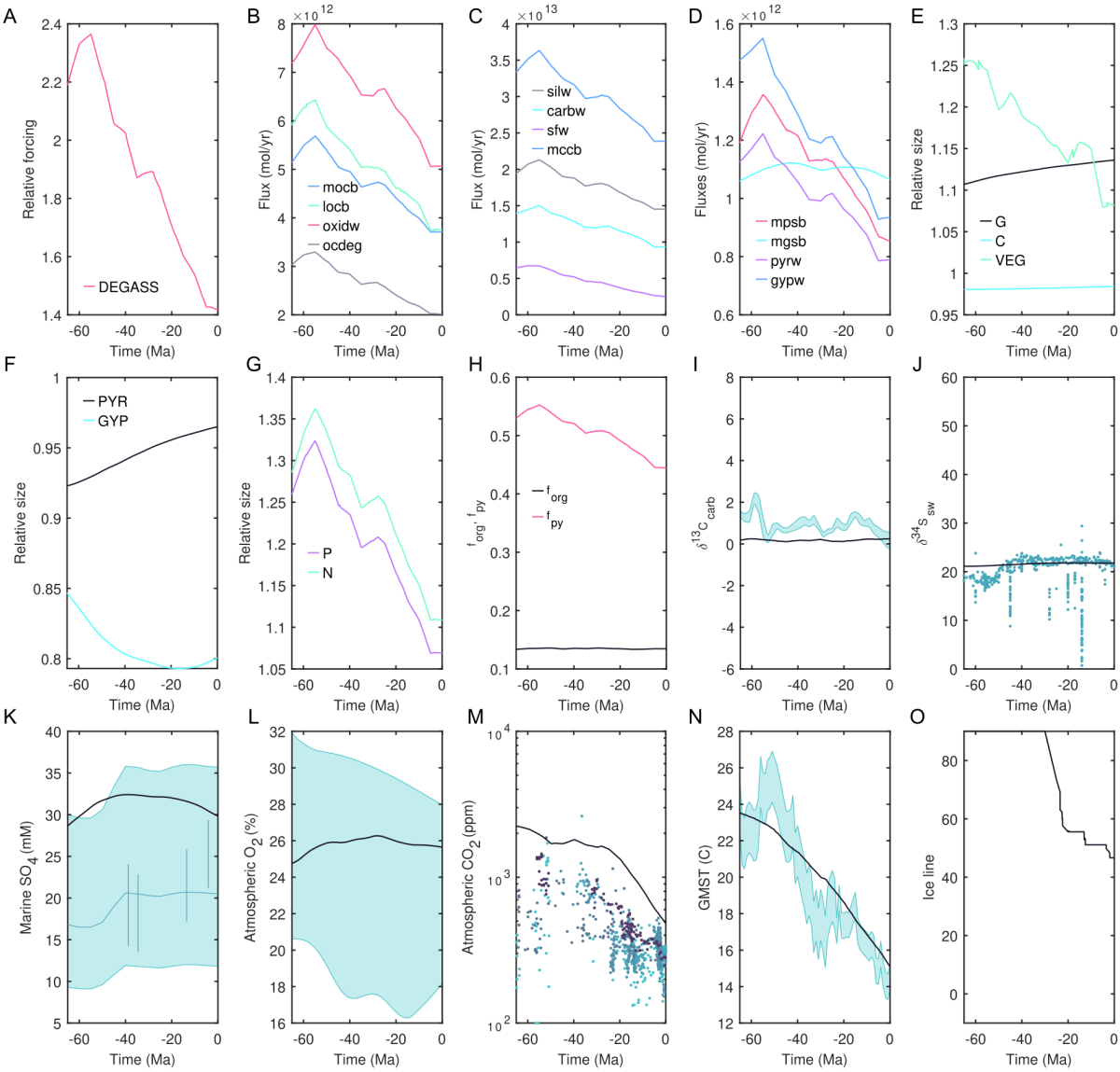


Figure S2. SCION model Cenozoic flux and atmosphere-ocean composition outputs. Panels A–H show model fluxes where *mocb* = marine organic carbon burial, *locb* = land organic carbon burial, *oxidw* = oxidative weathering, *ocdeg* = organic carbon degassing, *silw* = silicate weathering, *carbw* = carbonate weathering, *sfw* = seafloor weathering, *mccb* = marine carbonate carbon burial, *mpsb* = marine pyrite sulfur burial, *mgsb* = marine gypsum sulfur burial, *pyrw* = pyrite weathering, *gypw* = gypsum weathering, G = crustal organic carbon, C = crustal carbonates, VEG = relative vegetation biomass, PYR = crustal pyrite, GYP = crustal gypsum, P = marine phosphate, N = marine nitrate, f_{org} = fractional organic carbon burial, f_{py} = fractional pyrite sulfur burial. Panels I–N show proxy comparisons where proxies are in blue and model is in black. Proxy records derive from previous studies [5, 7–12].

These inconsistencies are emblematic of a field in which Cenozoic surface temperature evolution, and the relationship between temperature and CO_2 levels, have not yet been completely agreed [13], or reproduced in a forwards model like SCION. However, the purpose of the present SCION runs is to map a best-guess and self-consistent reconstruction of surface temperature and vegetation over the Cenozoic, which has been achieved. Above-proxy CO_2 levels here (which fertilize the vegetation) are countered by high O_2 levels (which limit the vegetation through photorespiration and wildfire), and the overall trend of Cenozoic global biomass prediction is consistent with model where CO_2 and O_2 proxy records were closely matched [2]. For this study, SCION outputs are mapped onto a high-resolution grid using linear interpolation. This interpolation is compared to the raw SCION outputs in **Figure S3**, and **Figures S4** and **S5** show full interpolated Cenozoic maps for surface air temperature and vegetation biomass.

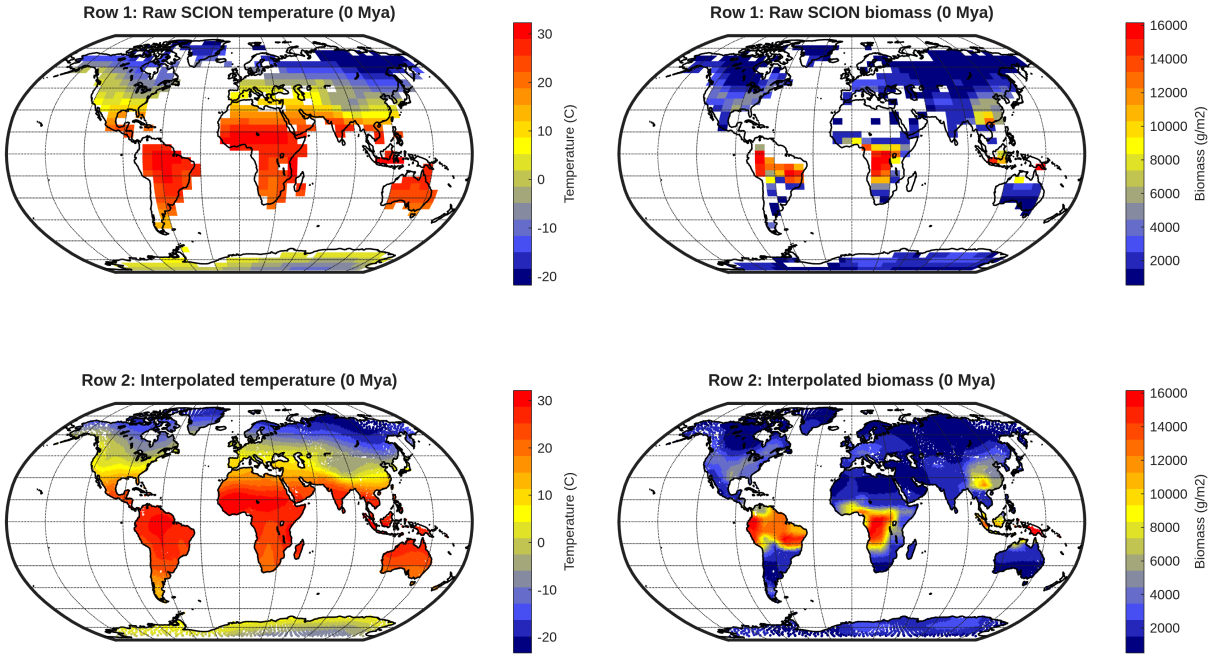


Figure S3. SCION model spatial outputs and interpolation.

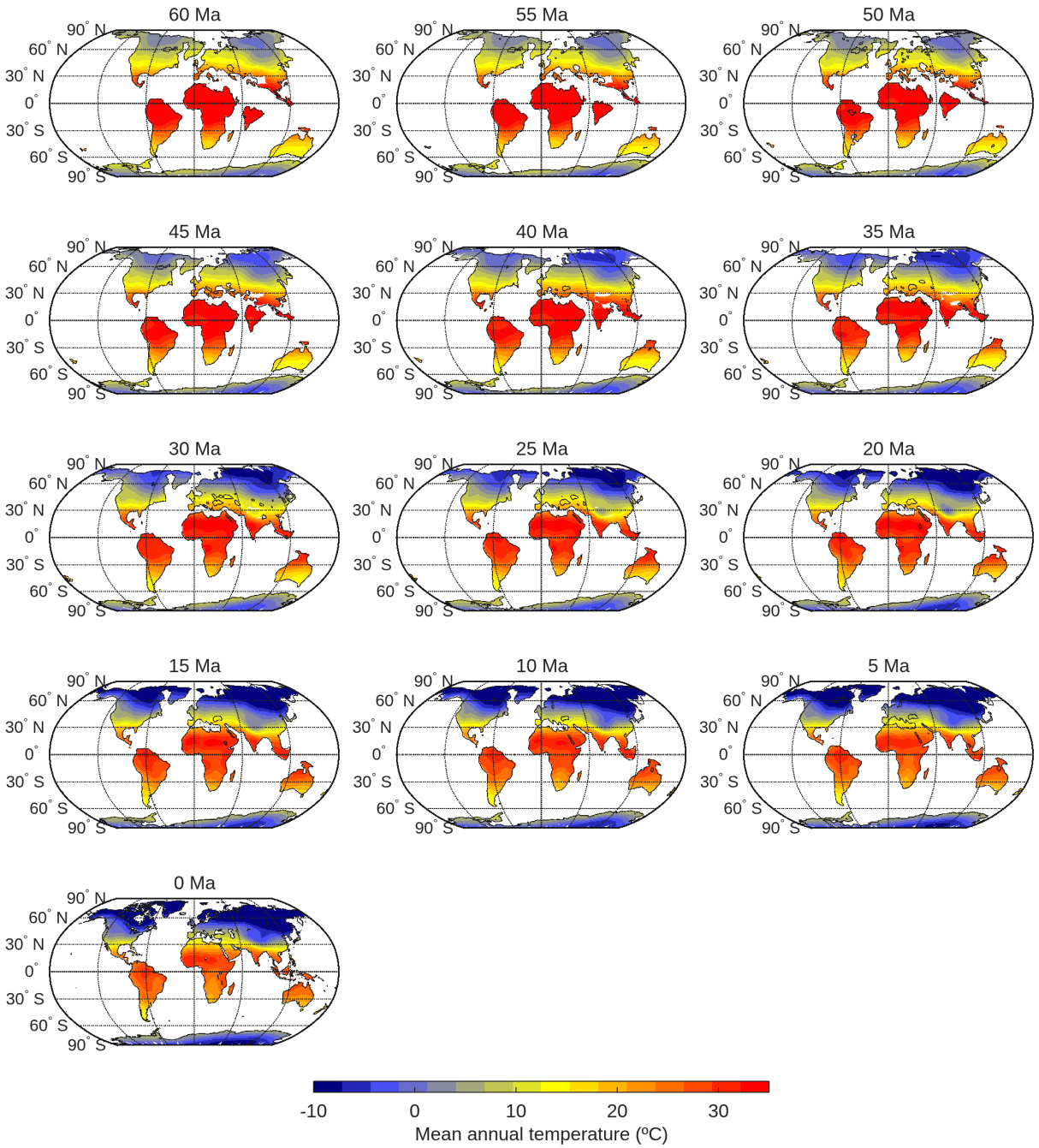


Figure S4. Interpolated SCION surface air temperature outputs.

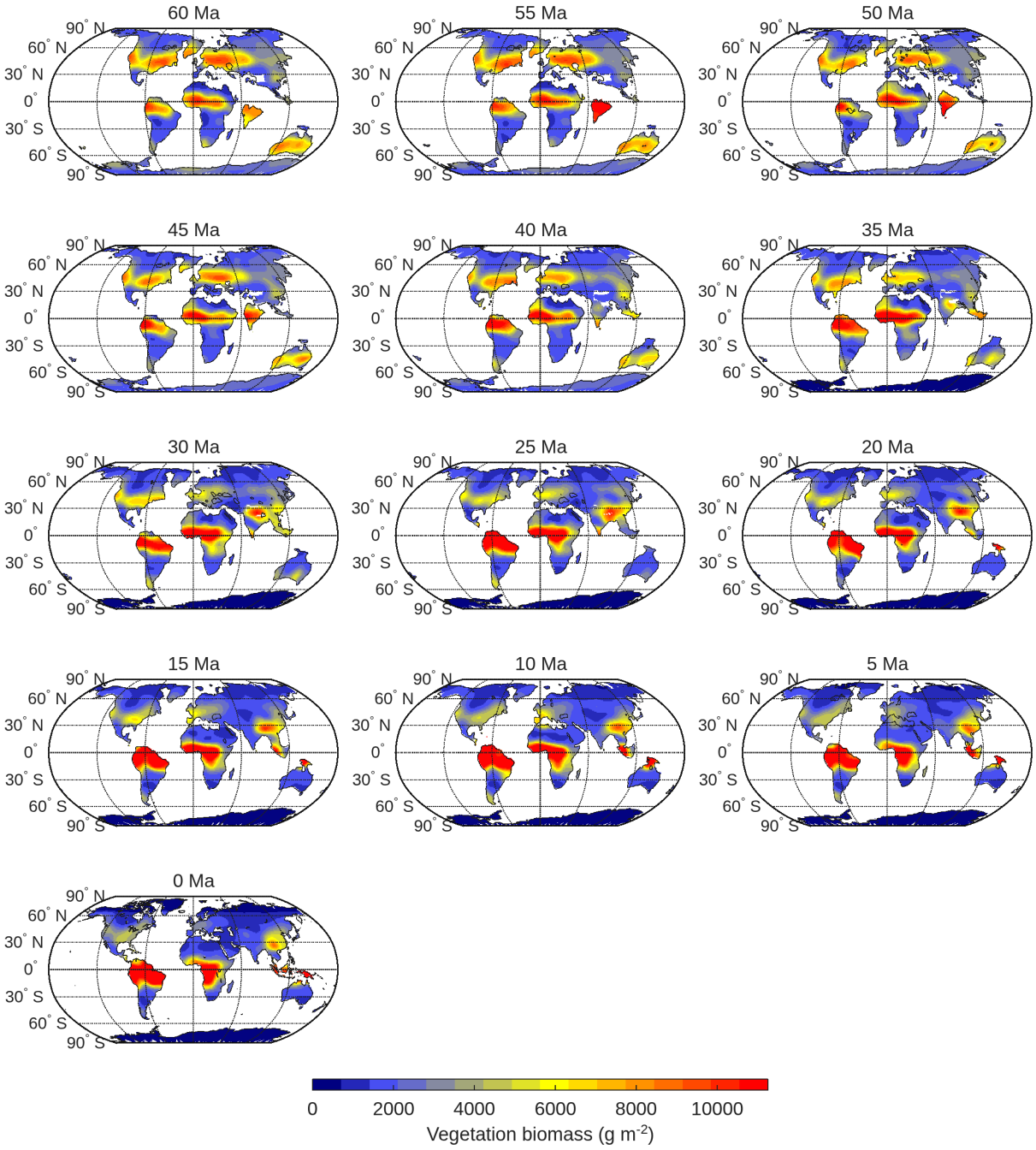


Figure S5. Interpolated SCION vegetation biomass outputs.

Climatic simulations

The continental weathering component of SCION requires a lookup table of surface temperature and continental runoff fields simulated using a general circulation model at several atmospheric CO_2 concentrations. A large lookup table of 1,090 new climatic simulations was generated to that purpose. This table consists in a gridded ensemble, the two axes of which are the continental configuration (varied between 540 Ma and 0 Ma every 5 Myr, for a total of 109 time slices) and the atmospheric CO_2 concentration (from 0.25 to 128 times the preindustrial atmospheric level of 280 ppm, incremented through CO_2 doubling for a total of 10 atmospheric CO_2 values).

The Fast Ocean Atmosphere Model (FOAM) version 1.5 is a mixed-resolution ocean atmosphere general circulation model [14]. The atmosphere is a parallelized version of the National Center for Atmospheric Research's (NCAR) Community Climate Model 2 (CCM2) benefitting from radiative and hydrologic physics upgrades after CCM3 version 3.2 [15]. In the ocean, we used a 50-meter "slab" mixed-layer model, whose quick integration time and time-to-equilibrium allowed us to conduct the 1,090 simulations of the lookup table. FOAM simulates sea ice using the thermodynamic component of the CSM1.4 sea ice model, based in turn on the Semtner 3-layer thermodynamic snow/ice model [16]. In terms of resolution, FOAM uses a R15 spectral resolution ($4.5° \times 7.5°$) with 18 levels in the vertical dimension in the atmosphere. The ocean has a higher resolution of $1.4° \times 2.8°$. Sea ice is simulated at the horizontal resolution of the ocean model. The model coupler, ensuring the communication between the ocean, atmosphere and sea-ice sub-models, also operates at the ocean resolution. FOAM has been widely applied to simulate palaeoclimates [17, 18], including in its slab-ocean setup [19, 20].

FOAM simulations were conducted for 109 time slices, between 540 Ma and 0 Ma every 5 Myr. For each time slice, palaeogeography was adapted, solar luminosity was calculated using the stellar physics of Gough [21], a null eccentricity-minimum (22°) obliquity orbital configuration was used providing an equal mean annual insolation to both hemispheres with minimum seasonal contrasts, and 10 atmospheric CO_2 concentrations were used (0.25, 0.5, 1, 2, 4, 8, 16, 32, 64 and 128 times the preindustrial atmospheric level of 280 ppm). Vegetation was varied in order to capture first-order changes in vegetation cover during the Phanerozoic. A rocky desert was used between 540 Ma and 460 Ma, tundra was imposed between 460 Ma and 380 Ma, a tropical evergreen, broadleaved forest between 380 Ma and 120 Ma, and a modern-like zonal vegetation cover between 120 Ma and 0 Ma. No land-ice cover was prescribed. Simulations were run for 100 years with monthly output, the last 50 years of which were used to build monthly climatology files.

Climate velocity, plate motion and thermal mismatch through time

The analyses in the main text summarise climatic stability over the full 60-Myr simulated interval. This supplementary section introduces **Figures S6**, **S7**, and **S8**, which show the underlying quantities for every 5-Myr interval: climate velocity ($\mathbf{v}_{\mathrm{clim}}$), tectonic velocity ($\mathbf{v}_{\mathrm{tec}}$), and the resulting thermal mismatch (M_{thermal}). Calculation details are given in the Methods of the main text.

Climate velocity

Climate velocity is the speed and direction at which a climate envelope moves across the Earth's surface (km Myr^{-1}) [22]. It is the local rate of temperature change divided by the local spatial temperature gradient, and so indicates how far, and in which direction, organisms would need to move to keep experiencing constant thermal conditions. By construction, $\mathbf{v}_{\mathrm{clim}}$ satisfies the

isotherm-displacement condition

$$\frac{\partial T}{\partial t} + \mathbf{v}_{\text{clim}} \cdot \boldsymbol{\nabla} T = 0, \tag{S1}$$

which states that an observer moving at $\mathbf{v}_{\text{clim}}$ experiences no change in temperature. Because the spatial gradient appears in the denominator, the same global temperature change can produce very different velocities in different places. For example, climate velocity becomes exceptionally high during rapid global cooling across flat continental interiors such as those of Eurasia and North America. There, the shallow temperature gradient means that a drop of a few degrees in temperature displaces the climate envelope hundreds to more than a thousand kilometres toward the equator within a geologically brief interval.

Plate motion as a modifier of climate velocity

Climate velocity is defined relative to fixed geographic coordinates. Over macroevolutionary time, however, the land carrying the biota is itself moving. Tectonic plates typically travel at 10–100 km Myr^{-1}, and exceptionally faster. Over tens of millions of years, this carries continents across tens of degrees of latitude, and therefore across climate zones, even without any change in global climate. On macroevolutionary time scales, the relevant quantity for biological lineages is not $\mathbf{v}_{\text{clim}}$ alone, but the velocity of the climate envelope relative to the plate beneath them, the vector difference or kinematic offset:

$$\Delta\mathbf{v} = \mathbf{v}_{\text{clim}} - \mathbf{v}_{\text{tec}}. \tag{S2}$$

When the plate drifts in the same direction as the shifting climate envelope, $|\Delta\mathbf{v}|$ is smaller than $|\mathbf{v}_{\text{clim}}|$, and tectonic transport partly or fully compensates for climate change. When the two move in opposite directions, $|\Delta\mathbf{v}|$ exceeds $|\mathbf{v}_{\text{clim}}|$, and continental drift adds to the thermal shift imposed by climate change.

Interplay of plate tectonics and climate velocity

The kinematic offset describes how fast the climate envelope moves relative to the plate, but not how much temperature change this produces. That depends on how steep the local temperature gradient is and on how the offset is oriented relative to it. Motion parallel to the isotherms, typically east–west, carries a parcel through little thermal change, whereas north–south motion carries it across successive isotherms. We therefore also quantify the thermal mismatch, M_{thermal}, the rate of temperature change actually experienced by a land parcel as it moves with its plate. Rather than deriving it from the velocity fields, we compute it directly as the first difference of temperature for the same material point between consecutive time slices (see **Methods**).

Figures S6 – S8 show, for each 5-Myr interval, maps of $|\mathbf{v}_{\text{clim}}|$, $|\mathbf{v}_{\text{tec}}|$, $|\Delta\mathbf{v}|$ and M_{thermal}, which the main text figures summarise across the full simulated interval. Comparing the panels for the same interval shows where drift compensated for climate change ($|\Delta\mathbf{v}| < |\mathbf{v}_{\text{clim}}|$) and where it amplified it ($|\Delta\mathbf{v}| > |\mathbf{v}_{\text{clim}}|$).

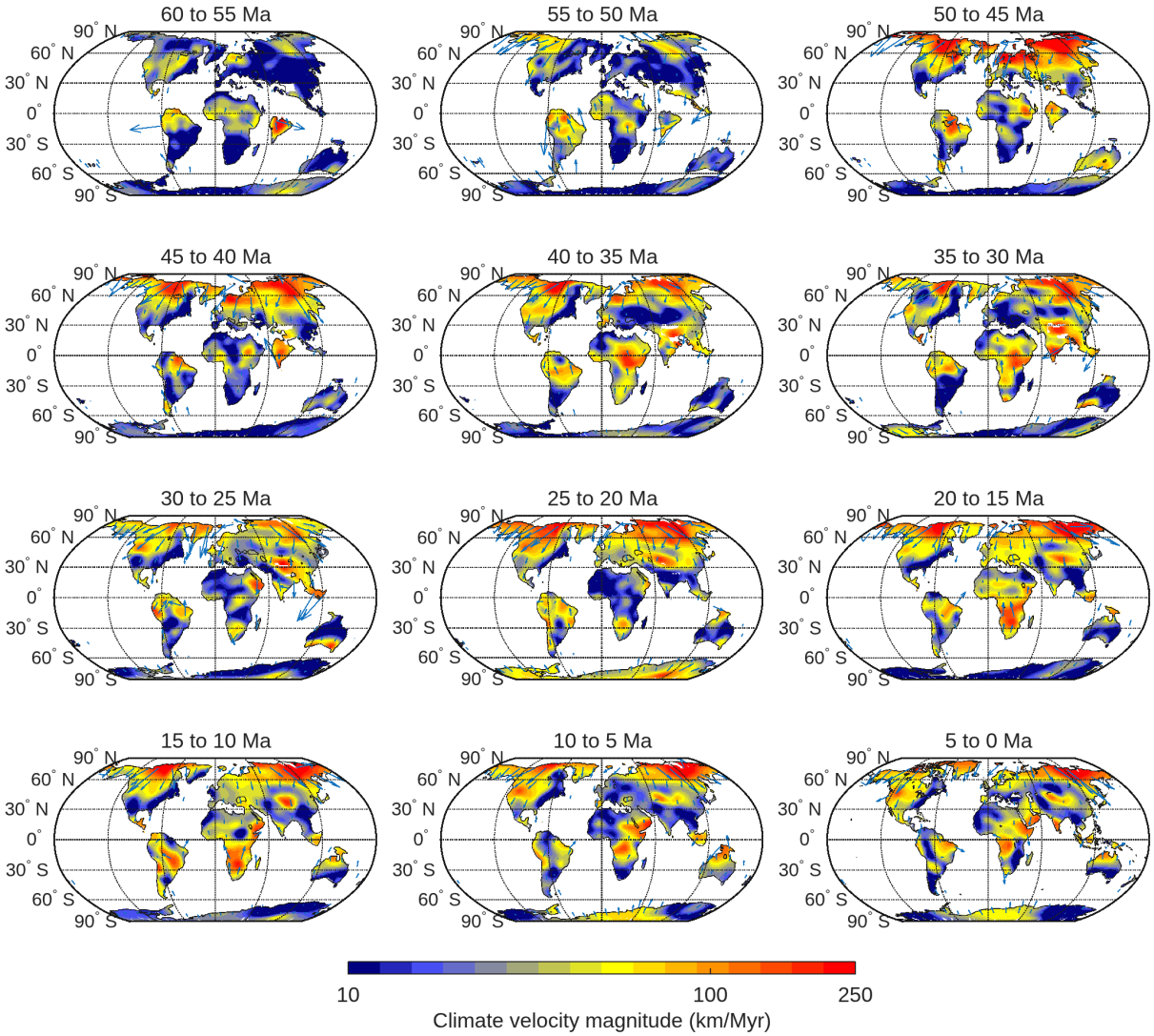


Figure S6. Global climate velocity maps from 60 Ma to present.

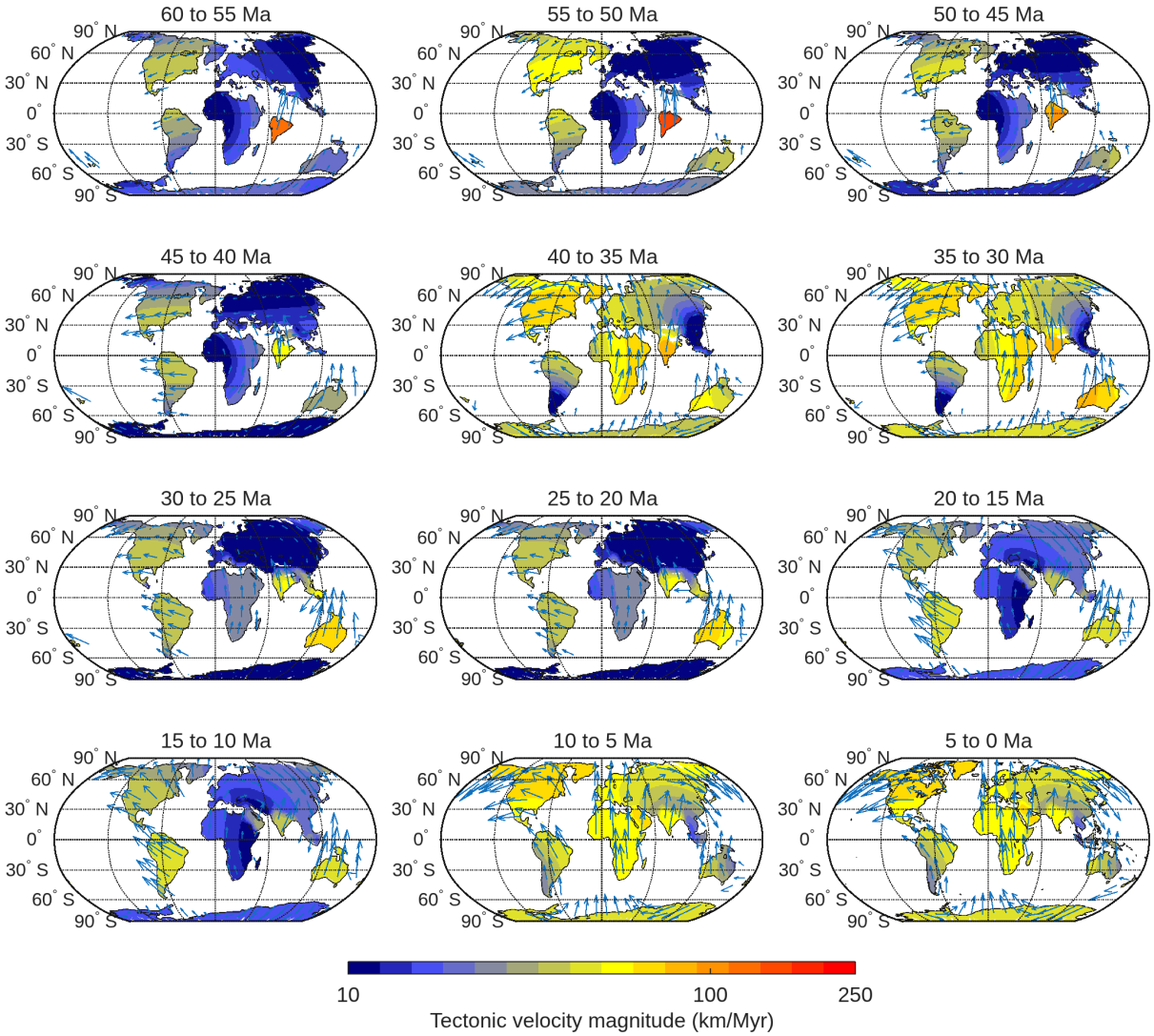


Figure S7. Global tectonic velocity maps from 60 Ma to present.

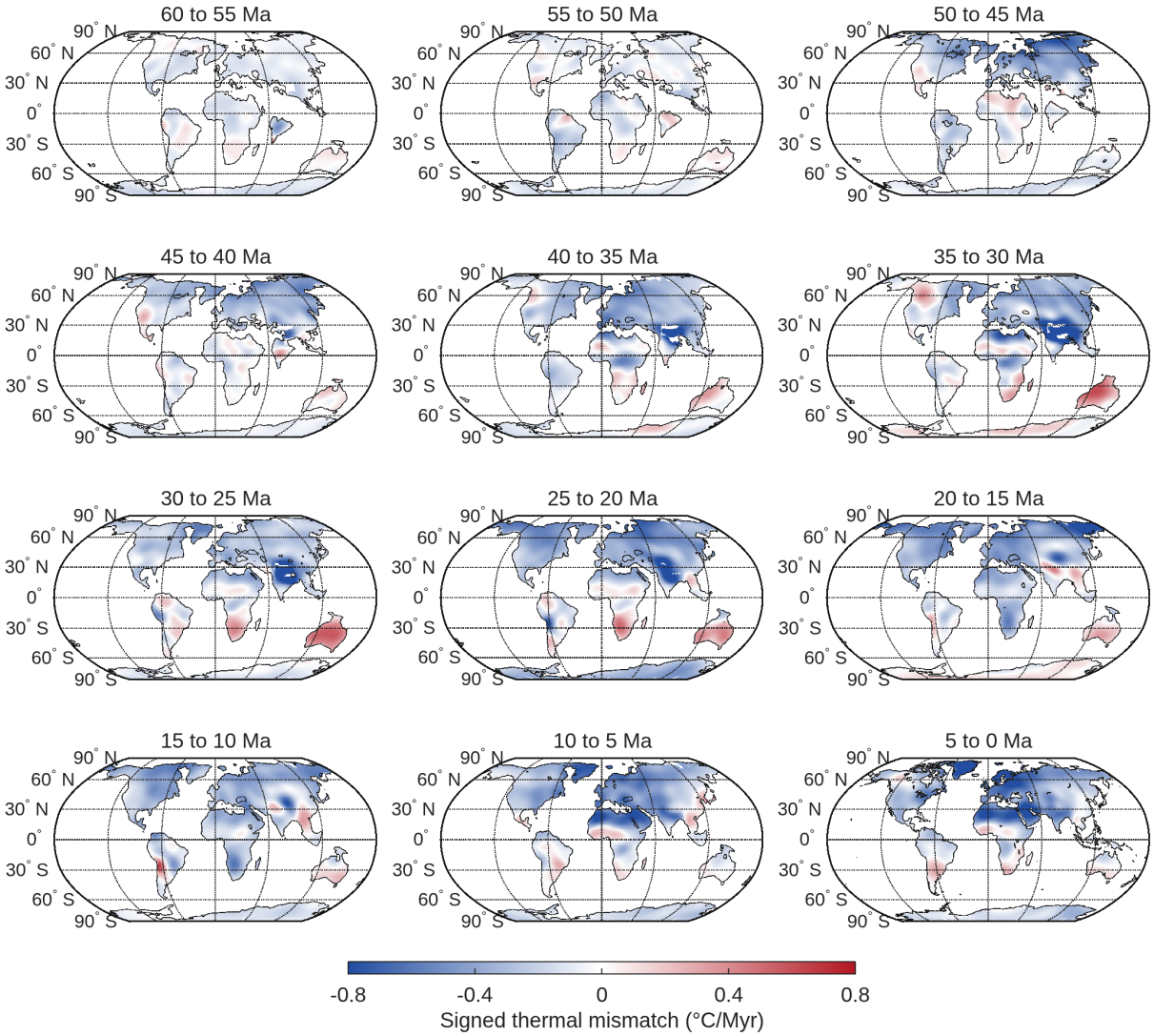


Figure S8. Global signed thermal mismatch maps from 60 Ma to present.

Choice of and sensitivity to the refugium threshold

Macroevolutionary refugia are defined as land whose cumulative stability (CS) exceeds a threshold θ. CS is a continuous quantity, so any choice of θ is partly arbitrary. We therefore (i) checked that the value used in the main text, $\theta = 20$ Myr, agrees with several independent criteria, and (ii) repeated the key analyses with $\theta = 15$, 20, 25 and 30 Myr.

Figure S9 shows the distribution of ensemble-mean CS across land parcels in the analysis domain. Each parcel is weighted by its area, so the histogram gives the share of land in each 1-Myr bin rather than the share of parcels. We compared two families of candidate thresholds:

- *Distribution-based criteria* locate a natural split in this distribution: the median, a two-class natural break (Jenks/Otsu) [23, 24], the midpoint of the central 95% of values, the upper tercile, the midpoint of the full range, the upper quartile, and the equal-posterior point of a two-component Gaussian mixture.

- *Model-based criteria* are fixed fractions (one-third and one-half) of the maximum CS attainable in the model, which is 60 Myr (twelve 5-Myr intervals from 60 to 0 Ma). These are independent of the observed distribution.

The distribution-based criteria fall within a narrow range, 16.2–22.2 Myr (blue band). The Gaussian-mixture split is the only exception. We excluded it from the band because the CS distribution is not bimodal (Ashman's $D < 2$), so a two-component mixture has no clear interpretation here. The model-based value of one-third of the maximum (20 Myr) also lies within the band. We adopted $\theta = 20$ Myr because it is close to the centre of the range supported by the data and has a simple interpretation: one-third of the 60-Myr record. The tested values of 15 and 25 Myr bracket the band, and 30 Myr (one-half of the maximum) is a deliberately strict upper bound.

Figure S10 shows how land classification changes as θ moves across the whole CS range. As expected, the share of land classified as refugia declines monotonically with θ, from about 58% at 15 Myr to about 9% at 30 Myr. Parameter uncertainty is shown in two ways:

- *Robust refugia* are parcels that remain above θ in at least 75% of the 100,000 ensemble members (ensemble $P_{25} > \theta$).

- *Ambiguous land* is land whose ensemble interquartile range straddles θ, so its classification depends on model parameters.

At $\theta = 20$ Myr, about 19% of land is robust refugia (roughly half of all refugia), and about 36% of land is ambiguous. The right-hand axis shows the share of refugia in which thermal continuity, rather than resource continuity, is the limiting factor. This share rises from about 38% at 5 Myr to 100% above about 34 Myr, and passes 50% near $\theta \approx 17$ Myr. The limiting mechanism therefore depends strongly on the choice of θ: resource continuity dominates at low thresholds and thermal continuity at high ones.

Refugia are defined by an upper-tail cut on a single continuous variable. As a result, raising θ only removes parcels and never adds new ones: the refugia at each higher threshold are a strict subset of those at the lower threshold (**Figure S11**). Changing θ therefore narrows the set of refugia toward their most stable cores, which lie in the Amazon basin, central and south-central Africa, and east-central China, with smaller cores in western North America. It does not move refugia to different regions. Conclusions that depend on where refugia are located are, for this reason, largely unaffected by the exact threshold.

We repeated the main-text comparison of protected-area coverage between refugia and other land for thresholds from 15 to 30 Myr (**Figure S12**). For each θ and each ensemble member, we calculated the share of each land class covered by protected areas and OECMs. We did this for all IUCN categories and separately for strict protection (categories I–IV). Across all thresholds,

mean coverage is higher in refugia than in other land. Coverage of refugia rises from about 20% at 15 Myr to about 31% at 30 Myr. Coverage of other land stays near 16%, below the global average of 17.8%. The gap Δ (refugia minus other land) grows from +5.3 percentage points at 15 Myr to +14.6 percentage points at 30 Myr. It is positive in 85% to 99% of ensemble members at the annotated thresholds. Strict protection shows the same pattern, but the gap is smaller: about 8–10% of refugia are covered, compared with about 7% of other land. Meanwhile, the area classified as refugia falls from 53% of land at 15 Myr to 9% at 30 Myr (bottom panel). The ensemble spread in refugia coverage widens as the class shrinks, and $P(\Delta > 0)$ falls slightly at the highest threshold, from 0.99 at 25 Myr to 0.94 at 30 Myr. Even so, the direction of the comparison holds across the whole tested range.

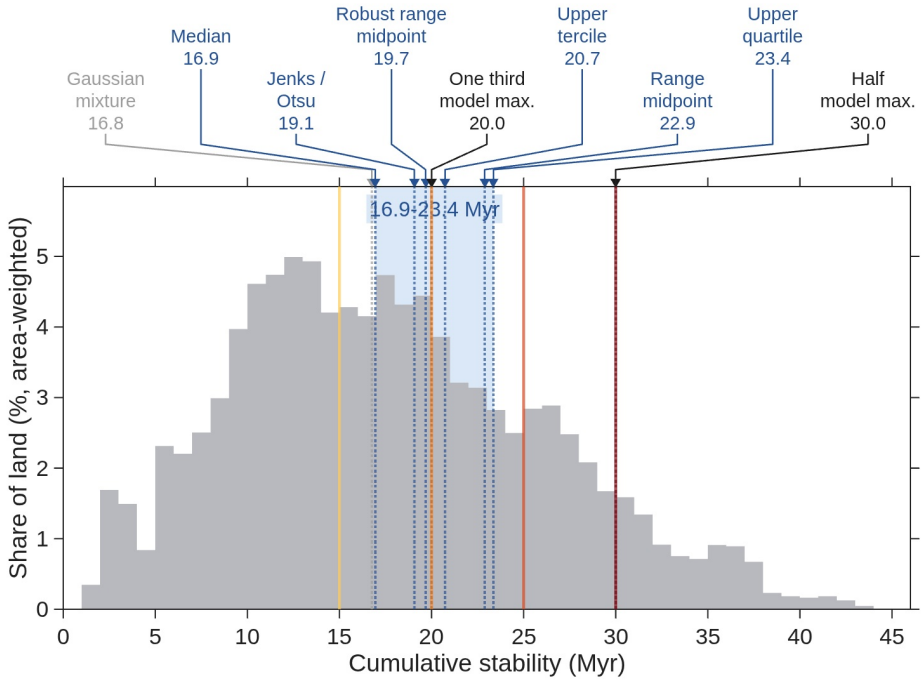


Figure S9. Justification of the 20 Myr cumulative stability threshold used to define macroevolutionary refugia. Distribution of cumulative stability across land parcels in the analysis domain, expressed as the area-weighted share of land per 1-Myr bin. Cumulative stability is the mean across the 100,000-member parameter ensemble. Dotted lines, with labelled markers on the top frame, show candidate thresholds from independent criteria. Distribution-based criteria (blue) are the median, a two-class natural break (Jenks/Otsu), the midpoint of the central 95% of values, the upper tercile, the midpoint of the full range and the upper quartile; together they span 16.2–22.2 Myr (blue band). The equal-posterior point of a two-component Gaussian mixture (grey) is excluded from the band because the distribution is not bimodal (Ashman's $D < 2$). Model-based criteria (black) are one-third and one-half of the maximum stability attainable in the model, 60 Myr (twelve 5-Myr intervals from 60 to 0 Ma). Solid coloured lines mark the thresholds tested in the sensitivity analyses (15, 20, 25 and 30 Myr).

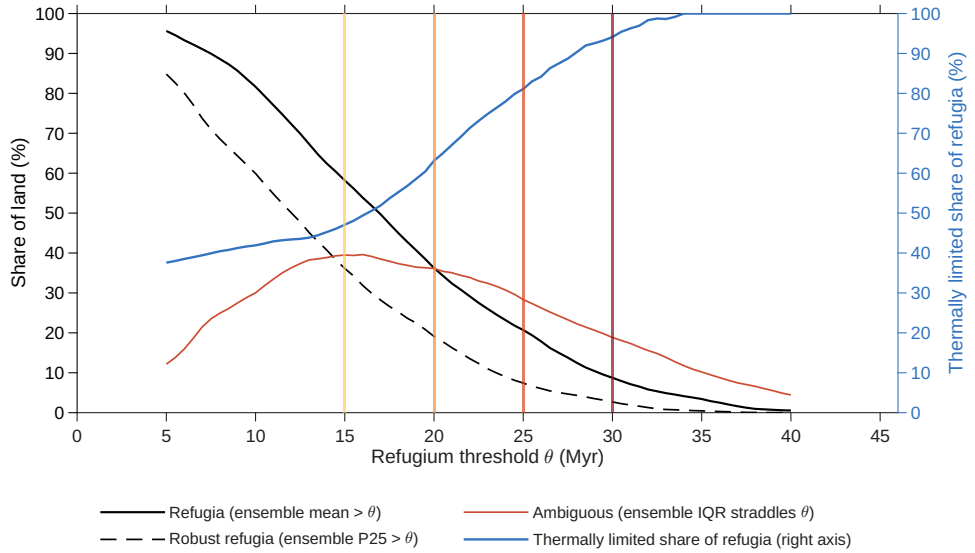


Figure S10. Land classification as a function of the refugium threshold. Curves show each class as a share of land. Refugia (solid black) are land whose ensemble-mean stability exceeds θ. Robust refugia (dashed black) are land that exceeds θ in at least 75% of parameter combinations (ensemble $P_{25} > \theta$). Ambiguous land (red) is land whose ensemble interquartile range straddles θ, so that its classification depends on model parameters. The blue curve (right axis) is the share of refugia in which thermal continuity, rather than resource continuity, is the limiting factor; parcels where the two continuities are equal are excluded. Vertical coloured lines mark the tested thresholds (15, 20, 25 and 30 Myr). The horizontal axis covers the same range as **Figure S9**.

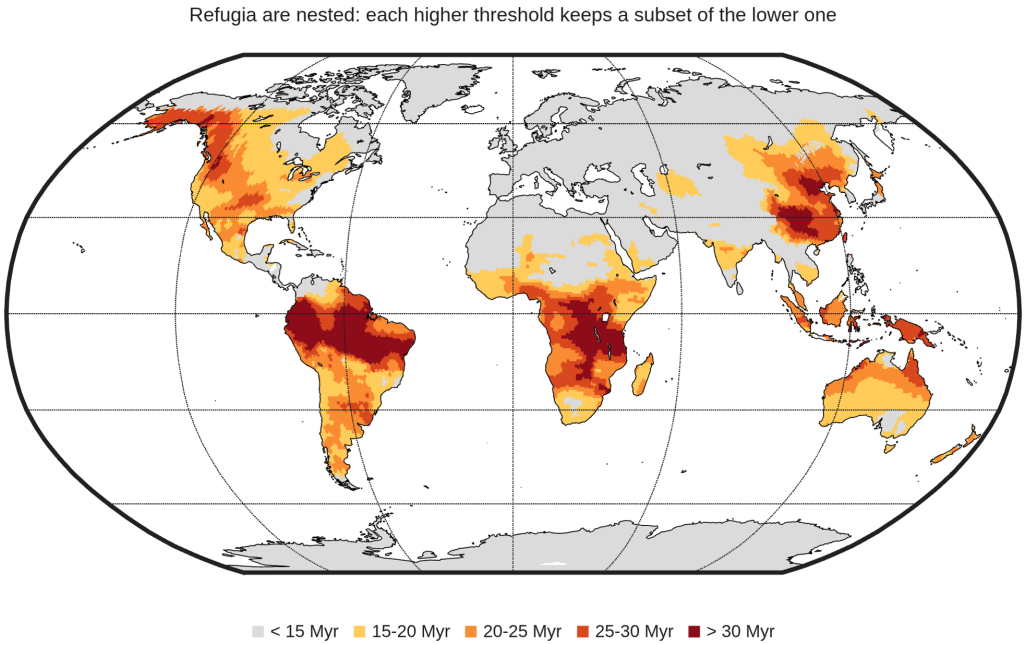


Figure S11. Refugia are spatially nested across thresholds. Each land parcel is coloured by the highest tested threshold that its ensemble-mean cumulative stability exceeds. Classes are < 15, 15–20, 20–25, 25–30 and > 30 Myr (grey to dark red, with the same colours as **Figures S9 and S10**). Because refugia are defined by an upper-tail cut, the refugia at each higher threshold are a strict subset of those at the lower one. The refugia used in the main text ($\theta = 20$ Myr) are the union of the three darkest classes. Parcel values were mapped onto a 0.5° grid by nearest-neighbour assignment, and cells further than 350 km from any parcel were left blank. The map is restricted to present-day land and drawn in a Robinson projection.

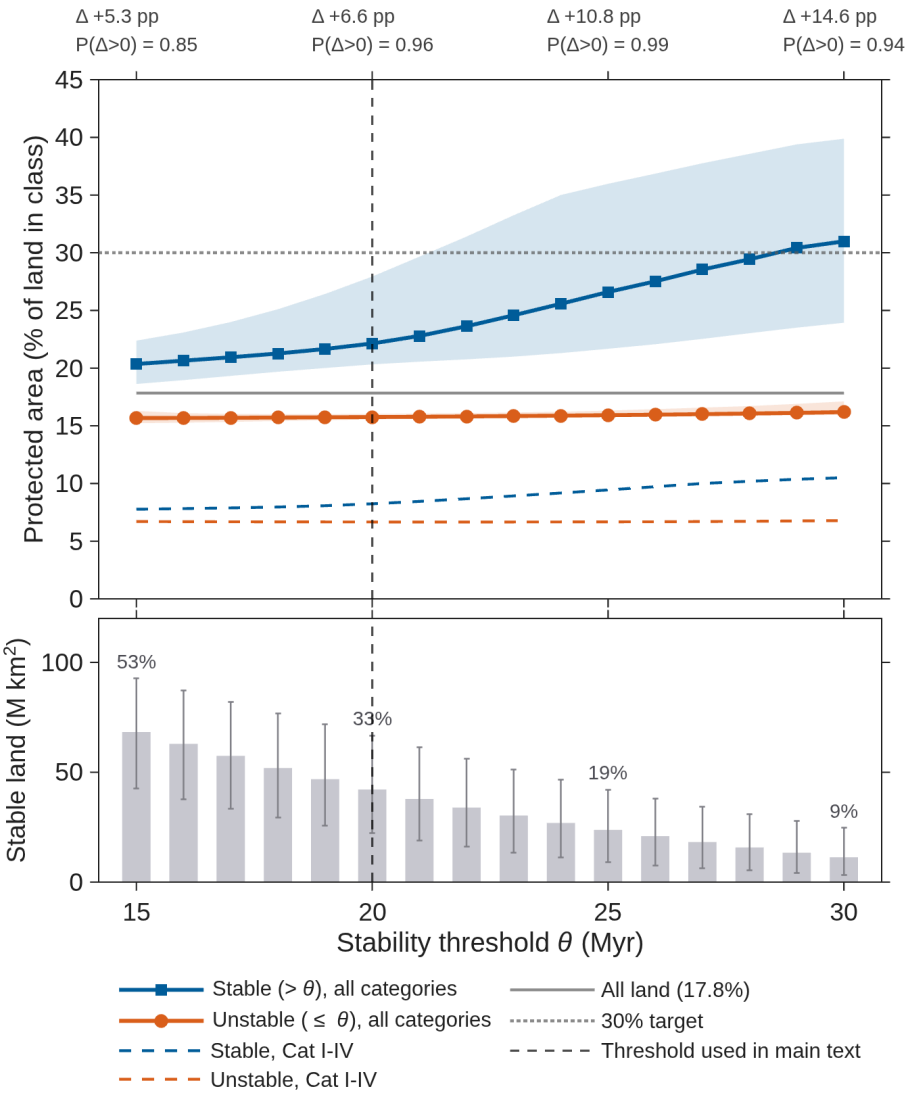


Figure S12. Sensitivity of protected-area coverage to the refugium threshold. *Top:* share of each land class covered by protected areas and OECMs (WDPA), as a function of θ. Stable land (refugia, CS $>\theta$) is shown in blue and unstable land (CS $\leq\theta$) in orange. Solid lines with markers show all protection categories and dashed lines show IUCN categories I–IV only. Lines show the ensemble median. Shaded bands show the 25$^{\text{th}}$–75$^{\text{th}}$ percentile range across ensemble members (all categories). The grey line gives coverage of all land, and the dotted line marks the 30% area-based target (Kunming–Montreal Global Biodiversity Framework, Target 3). Above the four annotated thresholds, Δ is the median coverage gap between stable and unstable land (percentage points, all categories), and $P(\Delta>0)$ is the share of ensemble members in which the gap is positive. *Bottom:* area of stable land (refugia) for each threshold. Bars show the ensemble median and error bars the 25$^{\text{th}}$–75$^{\text{th}}$ percentile range. Labels give the median as a percentage of total land area. The dashed vertical line in both panels marks the threshold used in the main text (20 Myr).

References

[1] Mills, B. J., Donnadieu, Y. & Goddéris, Y. Spatial continuous integration of phanerozoic global biogeochemistry and climate. *Gondwana Research* **100**, 73–86 (2021).

[2] Gurung, K., Field, K. J., Batterman, S. A., Poulton, S. W. & Mills, B. J. W. Geographic range of plants drives long-term climate change. *Nature Communications* **15**, 1805 (2024).

[3] Sitch, S. *et al.* Evaluation of ecosystem dynamics, plant geography and terrestrial carbon cycling in the LPJ dynamic global vegetation model. *Global Change Biology* **9**, 161–185 (2003).

[4] Scotese, C. R. & Wright, N. Paleomap paleodigital elevation models (paleodems) for the phanerozoic. PALEOMAP Project (2018). URL https://www.earthbyte.org/paleodem-resource-scotese-and-wright-2018/.

[5] Scotese, C. R. An atlas of Phanerozoic paleogeographic maps: The seas come in and the seas go out. *Annual Review of Earth and Planetary Sciences* **49**, 679–728 (2021).

[6] Merdith, A. S. *et al.* Extending full-plate tectonic models into deep time: Linking the Neoproterozoic and the Phanerozoic. *Earth-Science Reviews* **214**, 103477 (2021).

[7] Cramer, B. D. & Jarvis, I. Carbon isotope stratigraphy. *Geologic Time Scale 2020* 309–343 (2020).

[8] Crockford, P. W. *et al.* Claypool continued: Extending the isotopic record of sedimentary sulfate. *Chemical Geology* **513**, 200–225 (2019).

[9] Algeo, T. J., Luo, G. M., Song, H. Y., Lyons, T. W. & Canfield, D. E. Reconstruction of secular variation in seawater sulfate concentrations. *Biogeosciences* **12**, 2131–2151 (2015).

[10] Mills, B. J. W., Krause, A. J., Jarvis, I. & Cramer, B. D. Evolution of atmospheric o2 through the phanerozoic, revisited. *Annual Review of Earth and Planetary Sciences* **51**, 253–276 (2023).

[11] Foster, G. L., Royer, D. L. & Lunt, D. J. Future climate forcing potentially without precedent in the last 420 million years. *Nature Communications* **8**, 14845 (2017).

[12] Witkowski, C. R., Weijers, J. W. H., Blais, B., Schouten, S. & Sinninghe Damsté, J. S. Molecular fossils from phytoplankton reveal secular pCO_2 trend over the Phanerozoic. *Science Advances* **4**, eaat4556 (2018).

[13] Judd, E. J. *et al.* A 485-million-year history of Earth's surface temperature. *Science* **385**, eadk3705 (2024).

[14] Jacob, R. L. *Low frequency variability in a simulated atmosphere-ocean system.* Ph.D. thesis, University of Wisconsin–Madison (1997).

[15] Kiehl, J. T. *et al.* The national center for atmospheric research community climate model: CCM3. *Journal of Climate* **11**, 1131–1149 (1998).

[16] Semtner, A. J. A model for the thermodynamic growth of sea ice in numerical investigations of climate. *Journal of Physical Oceanography* **6**, 379–389 (1976).

[17] Pohl, A. *et al.* Glacial onset predated late ordovician climate cooling. *Paleoceanography* **31**, 800–821 (2016).

[18] Hearing, T. W. *et al.* An early cambrian greenhouse climate. *Science Advances* **4**, eaar5690 (2018).

[19] Nardin, E. *et al.* Modeling the early paleozoic long-term climatic trend. *GSA Bulletin* **123**, 1181–1192 (2011).

[20] Pohl, A. *et al.* Why the early paleozoic was intrinsically prone to marine extinction. *Science Advances* **9**, adg7679 (2023).

[21] Gough, D. O. Solar interior structure and luminosity variations. *Solar Physics* **74**, 21–34 (1981).

[22] Loarie, S. R. *et al.* The velocity of climate change. *Nature* **462**, 1052–1055 (2009). URL https://doi.org/10.1038/nature08649.

[23] Jenks, G. F. The data model concept in statistical mapping. *International Yearbook of Cartography* **7**, 186–190 (1967).

[24] Otsu, N. A threshold selection method from gray-level histograms. *IEEE Transactions on Systems, Man, and Cybernetics* **9**, 62–66 (1979).